Chapter 6

Systematic Uncertainty Descriptions and Estimates

In this chapter the systematic uncertainties related to the measurement of $P_\mu\xi$ are estimated. The method of estimating systematic errors is described in the anaysis overview in Section **??**.

The overall systematic uncertainty is estimated as the quadrature sum of individual sensitivity measurements S_i divided by a scale factor. The scale factor comes from the RMS change (σ_i) in the systematic effect in data over the change R_i introduced to measure the sensitivity to the systematic effect. The total systematic uncertainty is thus equal to:

$$\epsilon_{sys}^{tot} = \sqrt{\sum_i \frac{\sigma_i^2}{R_i} S_i} \tag{6.1}$$

The detailed listing of the systematic uncertainties is in Table 6.1. The total systematic uncertainty of $\pm 2.4 \times 10^{-3}$ is obtained on this measurement of $P_\mu\xi$.

In many cases the error in the sensitivity measurement was larger than the sensitivity, such that a real sensitivity was not measured. For those cases the random value that we got for the sensitivity was used in the same way as the rest of the measured sensitivies. It is expected that on average this method should give the best statistical estimate of the systematic uncertainty.

It should be noted that every effort was made to try to avoid double counting of the systematic error by separating effects into orthogonal errors. Inevitably there will be some overlap that cannot be avoided, ergo the error quoted in this thesis is believed to be greater or equal to the real systematic error.

The following sections discuss in detail the systematic errors categorized as positron interactions, spectrometer alignment, chamber response, momentum calibration, and muon beam.

6.1 Systematic Error Due to Muon Beam and Polarization

In bringing muons to a stop at the center of the $\mathcal{TWIST}$ spectrometer, muons can be depolarized by the combination of multiple scattering and interaction with the fringe field of the spectrometer, and by spin relaxation or other interactions in the vicinity of the muon stopping target.

This section will discuss the systematic uncertainty due to:

- muon depolarization in the production target,
- muon injection through the solenoid fringe field,
- muon depolarization at the stopping location,
- beam contamination with sneaky unpolarized muons,
- beam intensity and coincident particles, and
- proton beam stability.

Category	Sensitivity S_i Value	S_i Error	Scale R_i/σ_i	Systematic Uncertainty
Muon beam and polarization				±1.75
Fringe Field				1.50
Depolarization in Stopping Target				0.85
Depolarization in Production Target				0.30
Beam Intensity	-3.0	1.7	11	-0.27
Background Muon Contamination	1.0	1.4	1	0.18
Chamber response				±1.08
t0 variations	8.9	2.3	10	0.89
Density	2.4	1.4	5	0.49
Foil bulges	2.2	1.4	10	0.22
Cell asymmetry	-0.2	1.4	1	-0.22
Dead zone	0.2	1.4	12	0.01
Up-down efficiency	1.9	2.3	10	0.19
Positron interactions				±1.00
Energy Loss	1.0	1.4	1	0.95
Hard Interactions				0.30
Outside Material	1.2	2.0	60	0.02
Momentum calibration				±0.54
End point fits				0.54
B uniformity	-0.9	1.6	10	-0.09
Spectrometer alignment				±0.31
z	2.2	1.6	10	0.22
Rotations	8.5	1.6	39	0.22
B field to axis	1.2	1.4	40	0.03
Translations	0.1	1.6	28	0.00
Total Systematic Uncertainty				±2.4

Table 6.1: Table of Systematic Uncertainties in units of $\times 10^{-3}$

6.1.1 Depolarization in the Muon Production Target

The M13 beamline has $\Delta(p)/p$ of 1% (FWHM) meaning that we have a range of roughly 29.4 to 29.8MeV/c for our nominal beam of 29.6MeV/c. To get a conservative estimate of the depolarization in the production target we include a little extra for tails of the non-gaussian distribution. This is a range of 0.4MeV/c.

$\Delta(p)/\Delta(x)$ for this momentum is about 39.5$MeV/c/(g/cm^2)$ for Cu (similar to stainless steel) or 55$MeV/c/(g/cm^2)$ for carbon. Thus the difference in thickness corresponding to 0.4MeV/c, which is a good estimate of the effective maximum depth from which our muons are born, is 0.010g/cm^2 (ss) or 0.007g/cm^2 (graphite). Using densities of 8 and 2.26g/cm^3 respectively, the depths are 0.0012cm (ss) and 0.003 cm (graphite). Note that this is 30μm for the Graphite target.

Using the PDG multiple scattering formula, the multiple scattering angle in Graphite can be estimated. X_0 is 42.7g/cm^2, so $x/X_0 = 0.007/42.7 = 0.00016$, which is well below the quoted range of validity for the multiple scattering formula. Working it out anyways for $\beta = 0.265$ gives 0.0052 radians for $theta_0$.

An estimate of the depolarization in the small angle approximation, and averaging over phi angles which give a reduction of two times is estimated by $(\theta_0)^2/4$. This works out to a contribution $< 10^{-5}$.

6.1.2 Fringe Field Depolarization

In this section the sensitivity and systematic error of $P_\mu\xi$ due to uncertainty in beam position and angle is estimated. The uncertainty in beam measurement is estimated in the apparatus section describing the TEC. The uncertainty in the beam position was estimated to be $\pm 2mm$, and the uncertainty in the beam angle was estimated to be $\pm 5mrad$. While this seems like a fairly large uncertainty it is in line with discrepancies between the muon beam position in the detector in MC and data as shown in Figure 6.1.

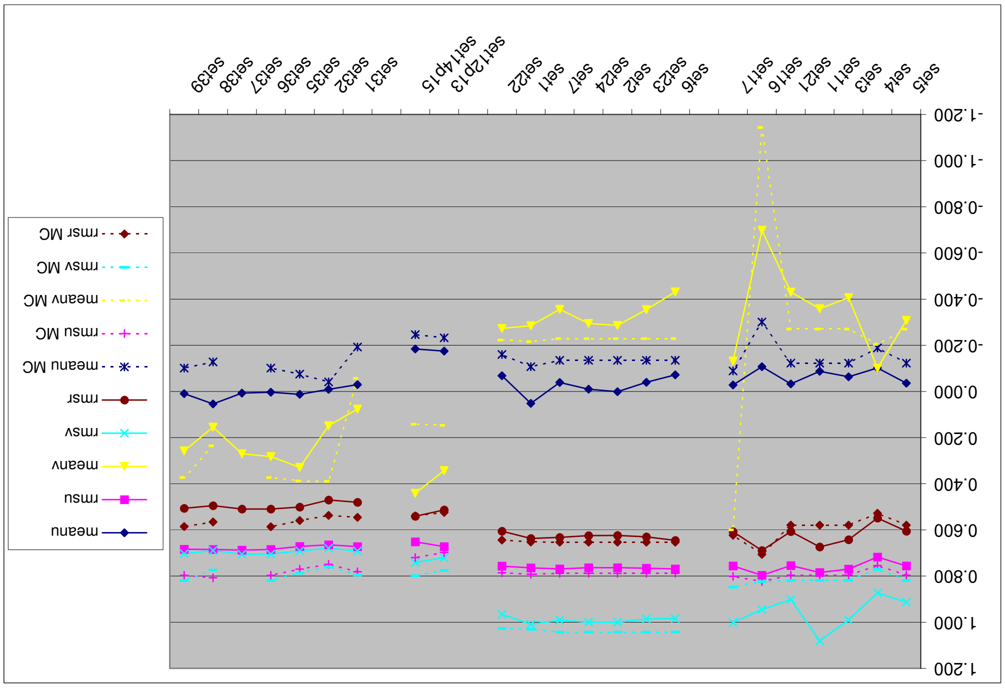

Figure 6.1: This plot shows the match between the mean beam positions and RMS at the stopping target. The match between the two is shown for each of the data sets being considered. Units on vertical scale are centimeters.

To estimate the sensitivity to fringe field depolarization, the beam input into MC was scanned over the range $\pm 2cm$ and $\pm 20mrad$ in both x and y. The result of this scan shows that the polarization versus beam shift can be approximated by a quadratic polynomial. The scan results are shown in Figure 6.2.

The quadratic that was fit to is given in Equation 6.2, where the x, y, dx and dy represent the shifts in the positions and angles.

$$P_\mu(x, y, dx, dy) = P_{max} - A((dx - x_0)^2 + (dy - y_0)^2) \tag{6.2}$$

The fit constants P_{max} and A were roughly independent of the shift in x and y, while the fit constants x_0 and y_0 were found to be functions of x and y.

Fits to x_0 versus x and y, and y_0 versus x and y can be done to find the constants in the linear equations:

$$x_0 = x_{00} + x_{0x}x \tag{6.3}$$
$$x_0 = x_{00} + x_{0y}y \tag{6.4}$$
$$y_0 = y_{00} + y_{0x}x \tag{6.5}$$
$$y_0 = y_{00} + y_{0y}y \tag{6.6}$$

The fits to these linear equations are shown in Figure 6.3.

The overall four dimensional polynomial can be written out:

$$P_\mu(x, y, dx, dy) = P_{max} - A((dx - x_{00} - x_{0x}x - x_{0y}y)^2 + (dy - y_{00} = y_{0x}x - y_{0y}y0)^2) \tag{6.7}$$

The constants in this polynomial for the standard beam tune are summarized in Table 6.2.

The four dimensional polynomial can be used to plot the sensitivity of the polarization to the estimated shifts in the beam. The result is that for an uncertainty in the beam position of $\pm 2mm$, and uncertainty in

Parameter	Nominal	Aperture	+5 Gauss	High Rate	Units
P_{max}	0.9958	0.9976	0.9950	0.9954	
A	-9.796	-10.536	-8.548	-9.831	$rad^{-}2$
x_{00}	0.0075	0.0067	0.0106	0.0075	rad
x_{0x}	-0.0129	-0.0121	-0.0142	-0.0133	rad/cm
x_{0y}	-0.0032	-0.0021	-0.0041	-0.0030	rad/cm
y_{00}	0.0058	0.0038	0.0167	0.0057	rad
y_{0x}	0.0024	0.0002	0.0020	0.0025	rad/cm
y_{0y}	-0.0137	-0.0122	-0.0149	-0.0138	rad/cm

Table 6.2: Beam polarization polynomial parameters from fit to MC scans of the different beam tunes.

Beam Tune	Nominal	Aperture	+5 Gauss	High Rate
Systematic Error	±0.0015	±0.0015	±0.0035	±0.0018

Table 6.3: Systematic error due to uncertainty in beam position and angle for each of the beam tunes used during 2004 data collection.

the beam angle of $\pm 5mrad$, the systematic error in $P_\mu\xi$ ±0.0015 for the nominal beam tune. The systematic error due to fringe field depolarization for the different beam tunes used in 2004 is summarized in Table 6.3.

The plot of the four dimensional polynomial used for this error estimate of nominal runs is shown in Figure 6.5.

6.1.3 Muon Depolarization at the Stopping Location

Introduction

This section will introduce physics mechanisms which could result in muon depolariazation due to interactions in material. Two contributions to the systematic error estimates due to material depolarization will be estimated. One for a possible shift in polarization due to stops in chamber gas, and another due to the extrapolation of a time dependent depolarizaton to zero decay time.

Mechanisms for Muon Depolarization in Materials

Down to about 30 keV the energy loss of muons is mainly due to ionization of atoms in the material it is traveling through. Below 30 keV, the thermalization of muons depends strongly on the material. In non-metals, the muons can be captured to form a bound state of a muon and an electron (Muonium, written chemically as Mu), which can have a spin exchange with the electron resulting in depolarization of the muons. In metals there is no Mu formation. Muons in metals will either stop at an interstitial site between metal atoms, or very rarely take the place of an impurity in the metal lattice. The conduction electrons, whose spins should align with the magnetic field act to screen the muon from Mu formation [19].

At the 99 percent level there is no depolarization in a high purity metal target if there is a huge holding field such as we have in TWIST. However at the 99.9 percent level it is less certain. The Muon creates a quasi-free state in Al where conduction electron concentration is $\simeq 2\times10^{23}cm^{-3}$. The polarized muon state is not stable because energy difference between parallel and anti-parallel spin states of muon in a $2T$ magnetic field is $\simeq 10^{-6}eV$ while thermal energy at $T = 300K$ is $kT \simeq 3\times10^{-2}eV$. Muon spin relaxation can only occur by interaction with the conduction electrons, nuclear moments of the Al, or with paramagnetic impurities in the metal. This section will present an analysis of the possible relaxation time dependence due to these interactions.

Interactions of muon spin with conductive electrons is called Korringa relaxation [60]. Conduction electrons create a large hyperfine magnetic field on muon. The hyperfine field produced at the muon can be considered as a fluctuating local field with a correlation time $\tau_c \simeq 10^{-13}s$ in Al [**?**]. This short correlation time results in a relaxation rate that has an exponential form. The Korringa relaxation rate does not depend on the magnetic field. Significant relaxation rates of $\lambda > 0.001\mu s^{-1}$ were obtained for muons in Cd, Sn, Pb, As, Sb, Bi [62]. The authors explained the measured relaxation rates to be due to Korringa relaxation because the λ value increases with temperature as predected. In our aluminum target at $H_L = 2T$ the measured muon relaxation rate of $\lambda = 0.00155\mu s^{-1}$ is most likely to be a Korringa exponential relaxation.

Nuclear moments of Al produce magnetic fields H_d of few gauss on a muon fixed in a crystal cell. According to many μ^+SR references the dipole-dipole interactions cause muon spin relaxation rates of $\lambda_d = 0.1$ to $0.3\mu s^{-1}$ in an orthogonal magnetic field. A longitudinal field H_L decreases the amplitude of the relaxation by the factor $(H_L/H_d)^2$ [63]. The amplitude at $H_L = 2T$ will be $< 10^{-6}$. The above is correct for muon fixed in a crystal cell. Diffusion motion of muon creates variable in 3D and time magnetic fields on a muon. As result muon relaxation rate drops and converts to an exponential dependence.

Our high purity aluminum stopping target has the following impurities in (ppm): Cu 0.3, Fe 0.3, Mg 1.2, and Si 0.8. Iron is the only paramagnetic impurity that can cause a relaxation. It is unlikely that this can cause much depolarization because we have only one Fe atom for every 3×10^7 atoms of Al. The probability for a muon to reach an Fe atom is very low. If a muon does reach the vicinity of an iron atom, then the electron magnetic moment on the muon of the Fe atom creates a magnetic field $H_e \simeq 1kG$ at distance of Al cell period of $\simeq 4\mathring{A}$. This magnetic field corresponds to a muon Larmor precession with frequency of $\omega_0 \simeq 10^8 s^{-1}$. The interaction causes a very fast muon relaxation of course if the muon fixed near the Fe, and Fe electron spin is fixed also. The spin of the iron impurity in Al fluctuates with time $\tau_c < 10^{-10}s$ [64]. The fluctuations decreases the relaxation rate, and the relaxation dependence becomes exponential form at $\omega_0 \cdot \tau_c \ll 1$ [63]. We have the $\omega_0 \cdot \tau_c \simeq 10^{-2}$. Therefore this unlikely interaction with an iron impurity causes an exponential relaxation. A relaxation rate of $\sigma \simeq 0.02\mu s^{-1}$ has been obtained in Al at $T > 100K$ with Fe admixture of $10ppm$ by Hartmann et. al. [65]. Our data also have $\sigma \simeq 0.02\mu s^{-1}$ when fitting to a gaussian depolarization rate. The depolarization rate independence in Al due to an increased iron concentration of 30 times is direct evidence that the measured muon relaxation rate is not due to the Fe impurity. The relaxation rate of Hartmann was measured in an orthogonal magnetic field. The rate independence from longitudinal versu orthogonal magnetic field up to $H_L = 2T$ is direct evidence of Korringa relaxation of the muon spin in Al.

High-energy muons creates defects in a matter. The paramagnetic defects can produce sufficient magnetic fields on a stopped muon. The electron configuration recovers in $\sim 10^{-11}s$ in metals [66]. The fast recovery means that this can only cause a fast muon relaxation. A muon can also displace atoms in a crystal cell. The displaced atom configuration changes very slowly. Average distance between a stopped muon and a last displaced atom in graphite, for example, is $9000\mathring{A}$ [67]. The effect of this interaction on the muon relaxation rate is negligible.

Materials in the Vicinity of the Muon Stopping Target

Introduction In the $\mathcal{TWIST}$ analysis, muons with a hit in PC6 and not in PC7 are considered to have stopped in the stopping target. While this is often the case, we can use our GEANT simulation to study how often we stop in other materials near the stopping target. The materials near the stopping target are the proportional chambers PC5 to PC8. Some muons will stop in each of the materials that the proportional chambers are made of: Aluminized Mylar foils (or 99.99% purity Aluminum between PC6 and PC7), CF4/i-C4H10 gas, and Gold plated Tungsten wires. A plot from MC of where the muon stops versus z coordinate reveals the fraction of muons stopping in different materials. We label the muon stopping fractions as f^i_j, where i=5,6,7 labels the selection of last proportional chamber hit by the muon, and j=Metal(m), Other(o), Gas(g), Plastic(p) labels the material. The label other is the sum of the fraction stopping in gas and plastic. Figure 6.6(a) shows the MC distribution in z of muons stopping in chambers around the stopping target, and (b) shows an expanded view of the muon stopping z coordinate for selection of PC5, PC6 and PC7 as the plane with largest z that has a TDC hit from the muon.

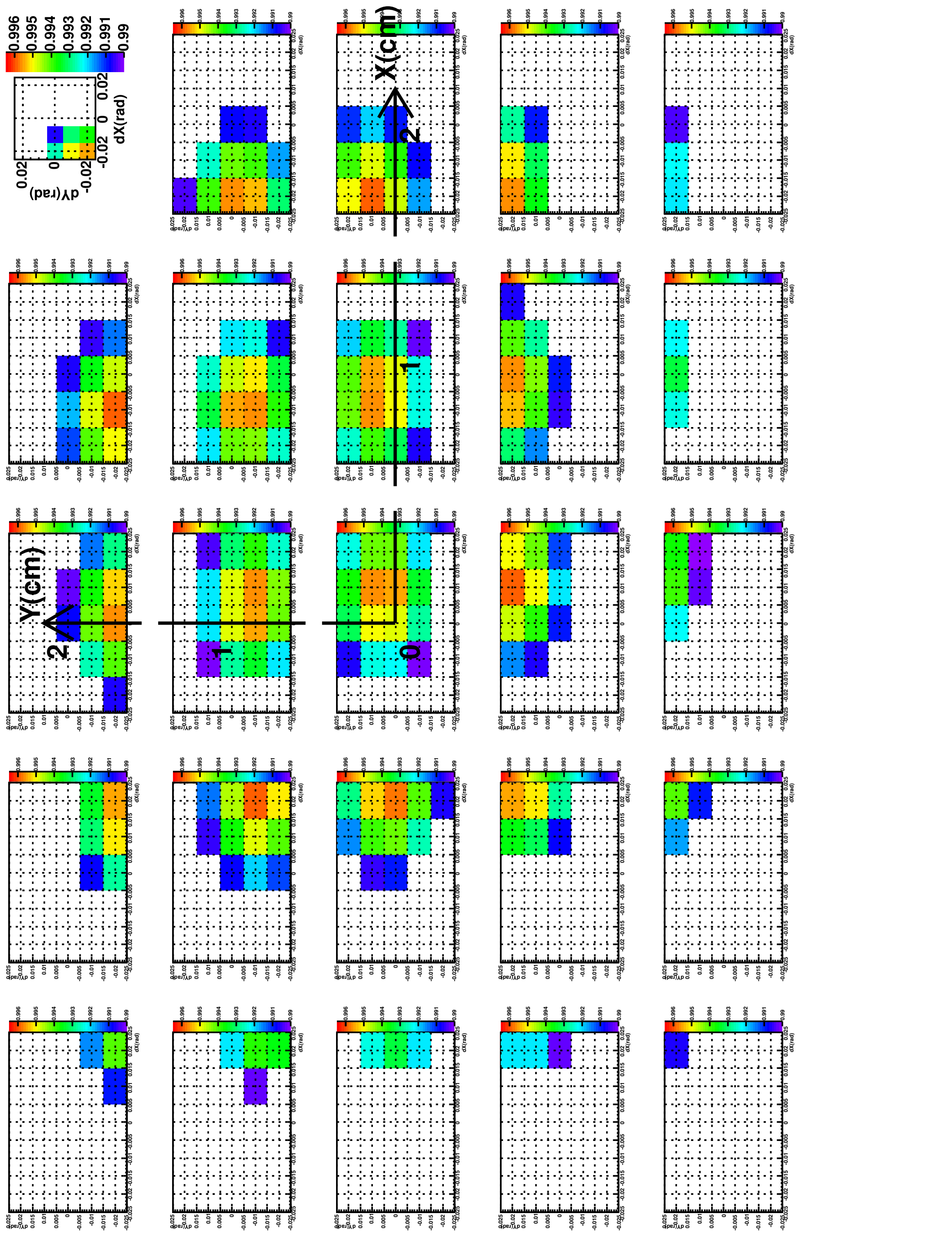

Figure 6.2: Fringe Field Sensitivity MC Scan showing the mean spin along the z axis for muons that stop in the target, where red is the highest polarization of 0.965, and blue is the lowest polarization of 0.99. An unshaded or white square is lower polarization than 0.99. Each of the 25 plots shown here is a polarization for each shift in dY versus dX from +20 mrad to -20mrad. The middle plot is for an unshifted beam, plots on the first row are for the beam shifted up by 2cm at the TEC, the second row shifted up by 1cm, and so on filling the matrix of beam shifts in X and Y from +2cm to -2cm.

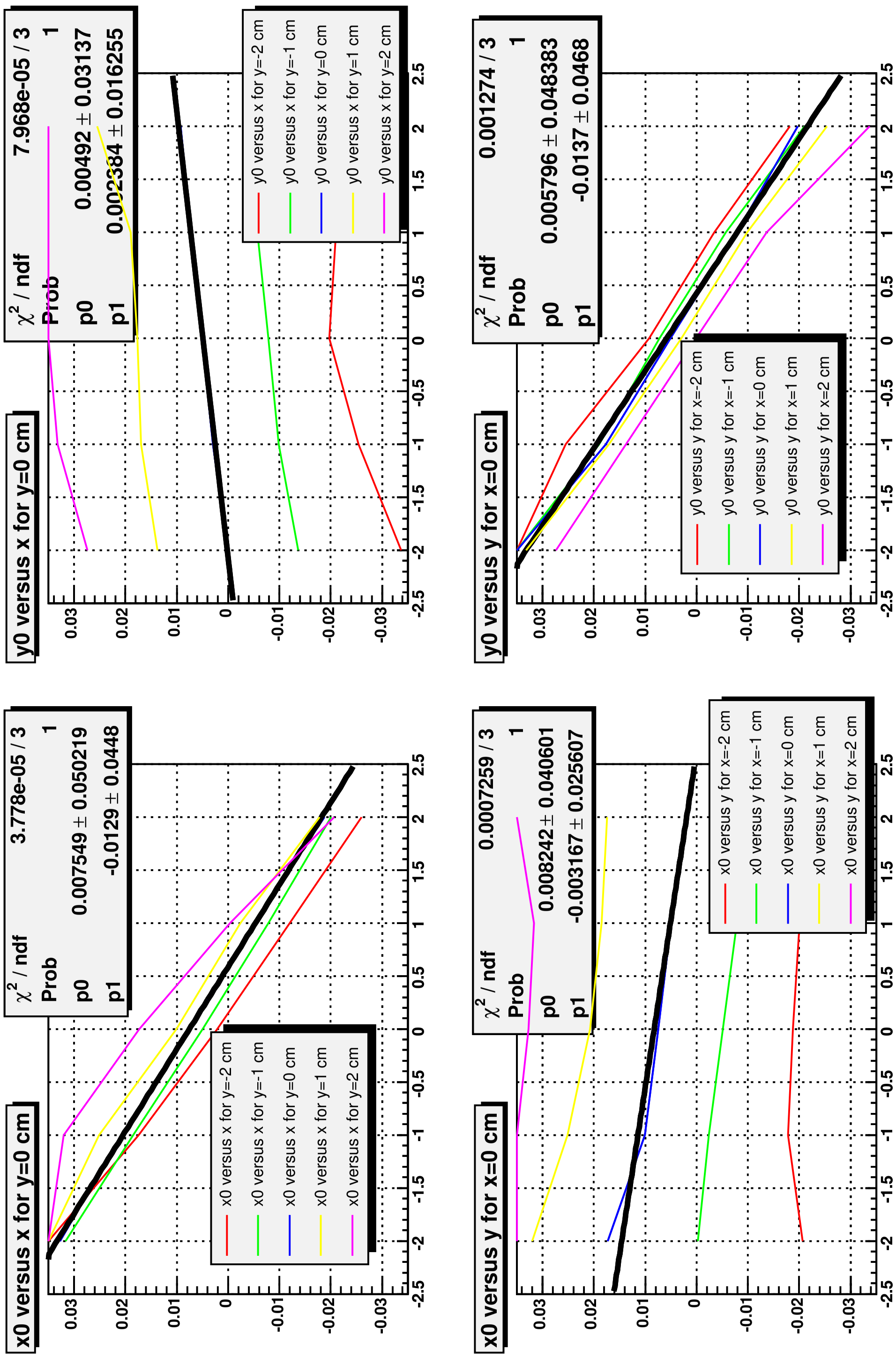

Figure 6.3: Fits of x0 versus x, x0 versus y, y0 versus x and y0 versus y used to obtain constants in the four dimensional polarization polynomial.

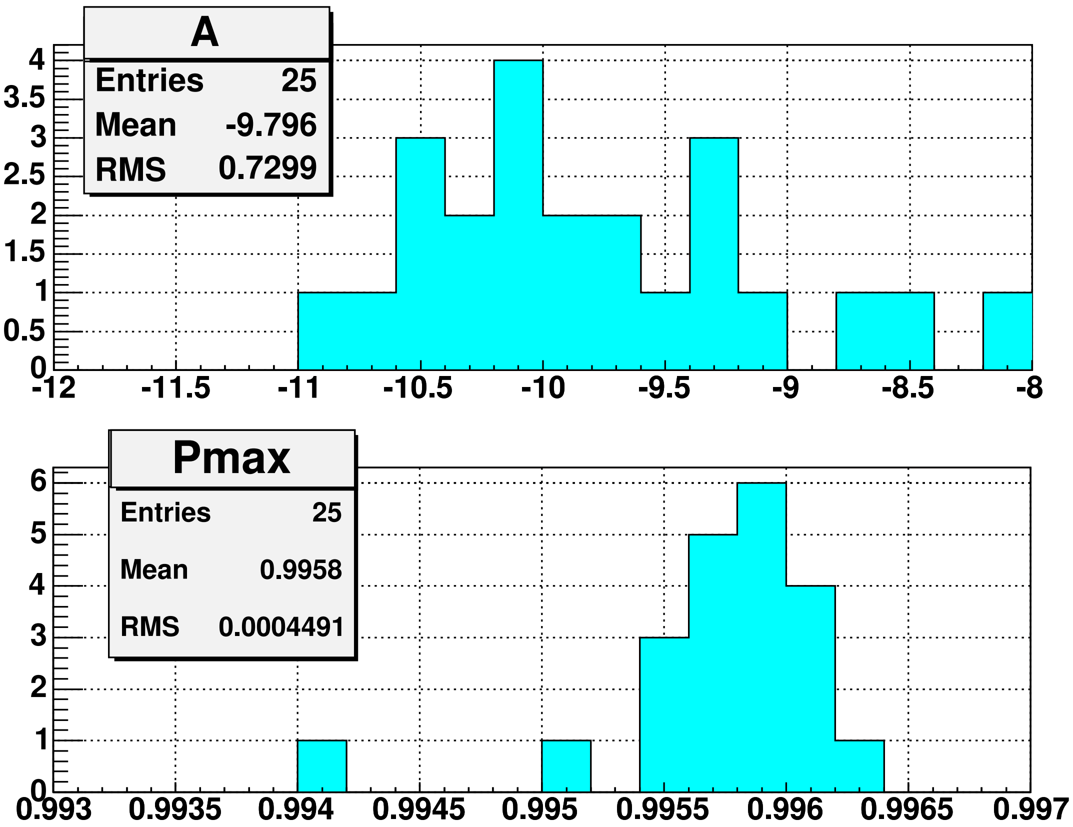

Figure 6.4: Histogram of the fit parameters A and pmax from fits to each of the 25 plots of polarization versus shift in dX and dY angle.

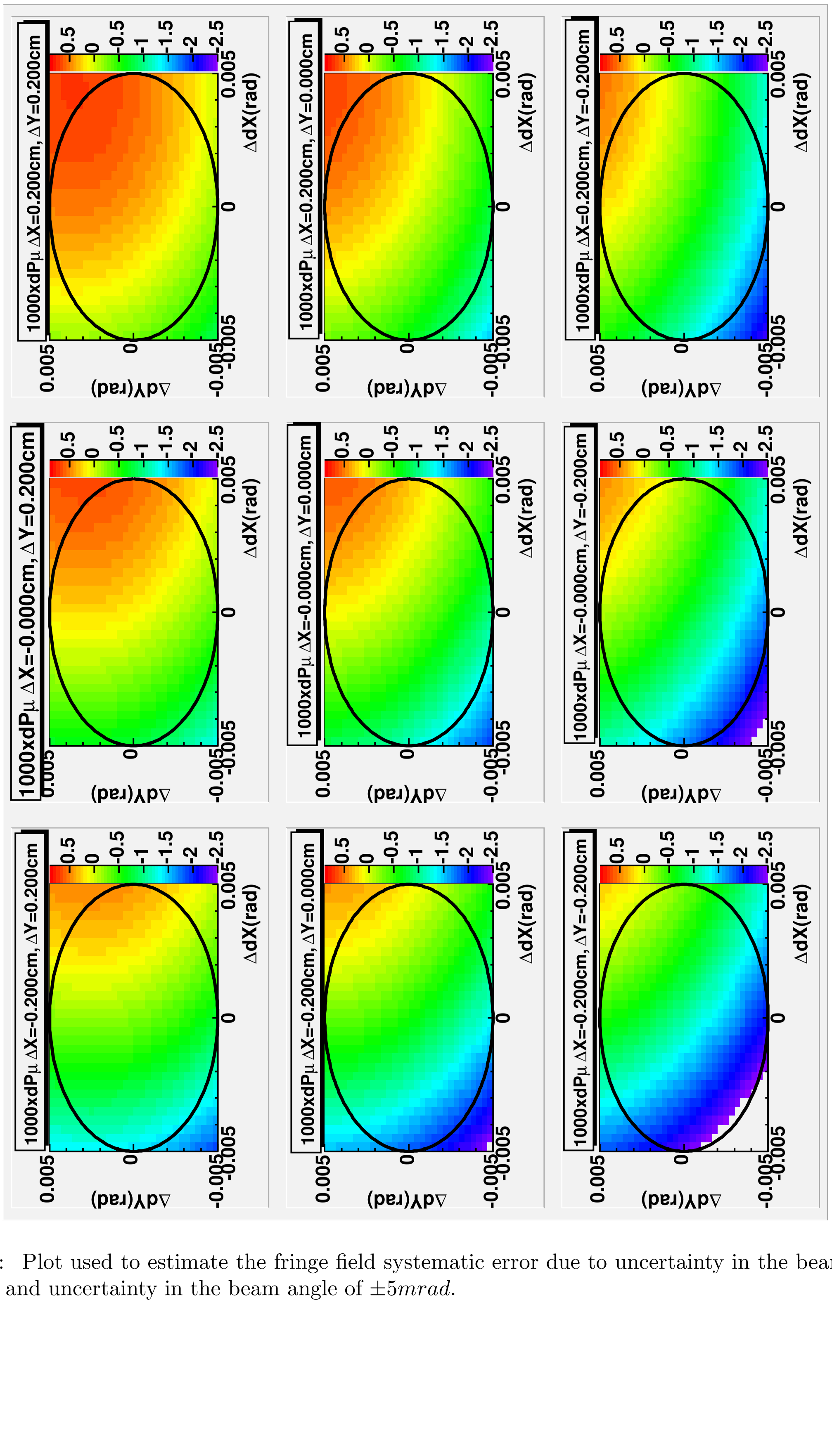

Figure 6.5: Plot used to estimate the fringe field systematic error due to uncertainty in the beam position of $\pm 2mm$, and uncertainty in the beam angle of $\pm 5mrad$.

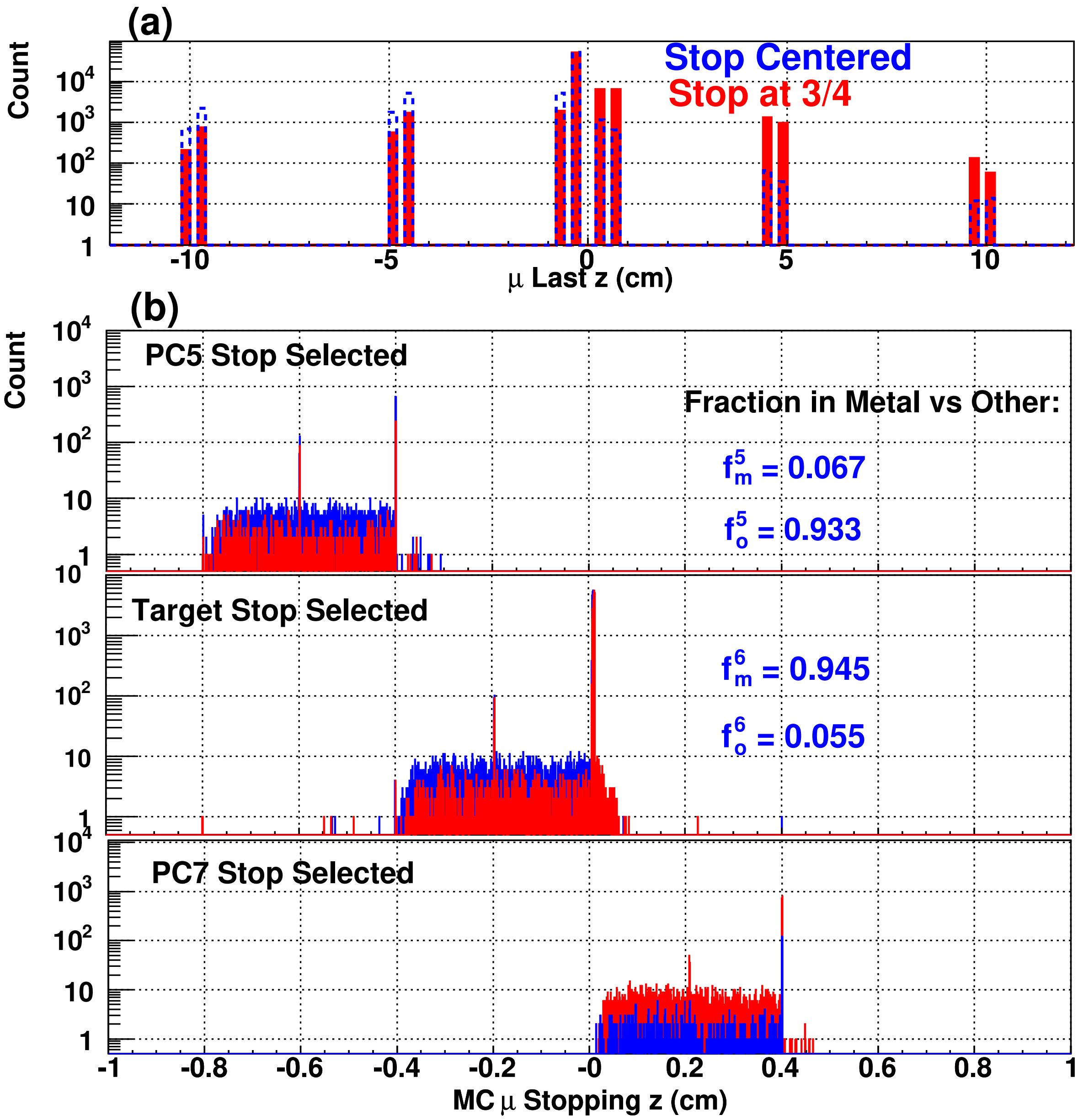

Figure 6.6: (a) Shows the MC distribution in z coordinate of muons stopping in chambers around the muon stopping target. (b) Shows an expanded view of the muon stopping z coordinate for selection of PC5, PC6 and PC7 as the plane with largest z coordinate that has a TDC hit from the muon. The PC5 selected is at top, PC6 selected is in the middle, and PC7 selected is shown at the bottom. In both (a) and (b) muons with Bragg peak centered in the muon stopping target are shown in blue, and those stopping at 3/4 are shown in red.

By knowing the fraction of muons stopping in each material, and measuring P_μ from the muon decay spectrum from different selections of the muon's last plane hit, we can estimate how large this effect could be. Of course the fraction stopping in different materials depends on where the muon Bragg peak is centered. The stopping fraction in different materials when the muon's last hit was in PC 6 is shown in Figure 6.7. In that figure the fraction stopping from MC is plotted versus the mean muon stopping position from TDC information.

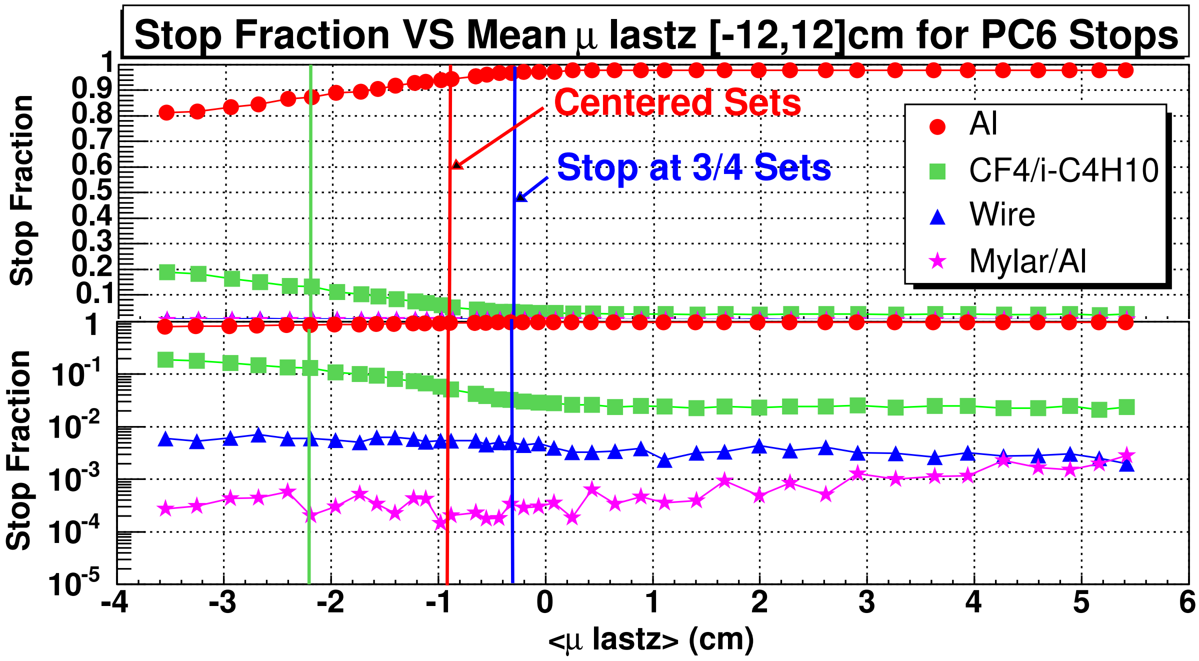

Figure 6.7: Plot of the fraction of muons stopping in Aluminum (Al), Gold plated Tungsten wire, CF4/i-C4H10, and Aluminized Mylar foil for muons with last TDC hit in PC6, versus the mean muon stopping z coordinate between -12.cm and 12.cm from TDC information. The mean muon stopping z coordinate for: data set 32 is shown as a green line, data sets with Bragg peak centered as a red line, and data sets stopping at 3/4 as a blue line.

Muon Depolarization at The Stopping Location

As pointed out eariler in ths section a depolarization versus decay time has been observed for muons stopping in our aluminum target. Plots of the polarization estimate from an asymmetry analysis of the 2004 data and MC are shown in Figure 6.8. The depolarization rate cannot be explained solely by muons that stop in gas rather than aluminum. Models for depolarization in metal are either of an exponential or gaussian form. Calculations have shown earlier in this section show that the only practical form is an exponential, since the effects of the other models cannot be very large.

The difference between the two model extrapolations is $2.4 \times 10^{-}3$, and this difference is the *correction* that we need to apply to our MC to data fits, since the MC was generated with a gaussian form, and we want to fit to an exponential form. An estimate of the extrapolation error is obtained by comparing fits with the slope as a fit parameter, and fits with the slope fixed as shown in Figure 6.9. The error due to extrapolation is: $\sqrt{0.00099^2 - 0.00049^2} = \pm 0.00085$.

6.1.4 Background Muon Contamination

A contribution to the depolarization is contamination from unpolarized background muons. Strong evidence for this is found in 2002 data where the muons were stopped further upstream than nominal. In this set a

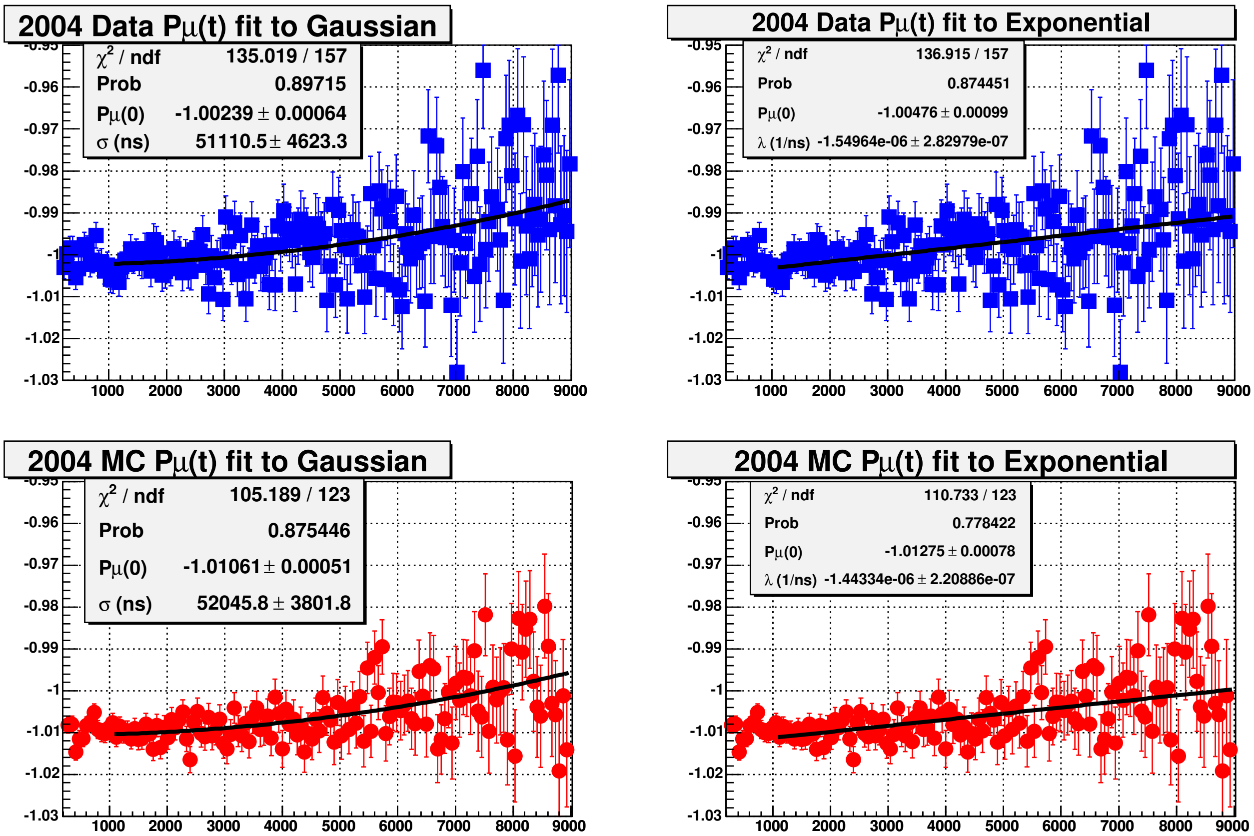

Figure 6.8: Plot of the polarization estimate from an asymmetry analysis of the 2004 data at the top, and 2004 MC at the bottom. The distributions are fit to a gaussian on the left and to an exponential on the right.

reduced polarization is observed for muons whose last hit was in PC7 or PC8.

It is expected that nearly all of the surface muons will stop in or before the target, meaning that the stops observed in PC7 and PC8 are likely due to these background muons. An estimate for the contamination is done in the following way. The data was modeled in GEANT as a combination of a standard geant run with polarized surface muons, and a special run with muons arising from 29.6MeV/c pion decays in channel. Figure 6.10 shows the comparison of MC and data distributions of muon last plane hit before and after adding pions to the beam.

Using these simulations, the fraction of muon stops due to the pions relative to surface muons is summarized for the 2002, 2003, and 2004 data in Table 6.4. The maximum polarization change is calculated for the case where the background muons have polarization opposite to surface muons. These estimates say that the systematic uncertainty in $P_\mu\xi$ due to background muons in 2003 and 2004 data is better than ± 0.00018.

Data Type	f_{PC5}	f_{target}	f_{PC7}	max ΔP_μ
2002 Nominal (Set 2)	0.009106	0.000364	0.000669	0.00072
2002 Upstream (Set 4)	0.009027	0.002793	0.012078	0.00240
2003 Nominal (Set 14)	0.000134	0.000013	0.000040	0.00003
2004 Nominal (Set 35)	0.001110	0.000088	0.000798	0.00018

Table 6.4: Fractions of background muons relative to surface muons for muons stopping in PC5, the target, and PC7. For the target stops the maximum effect on polarization is estimated.

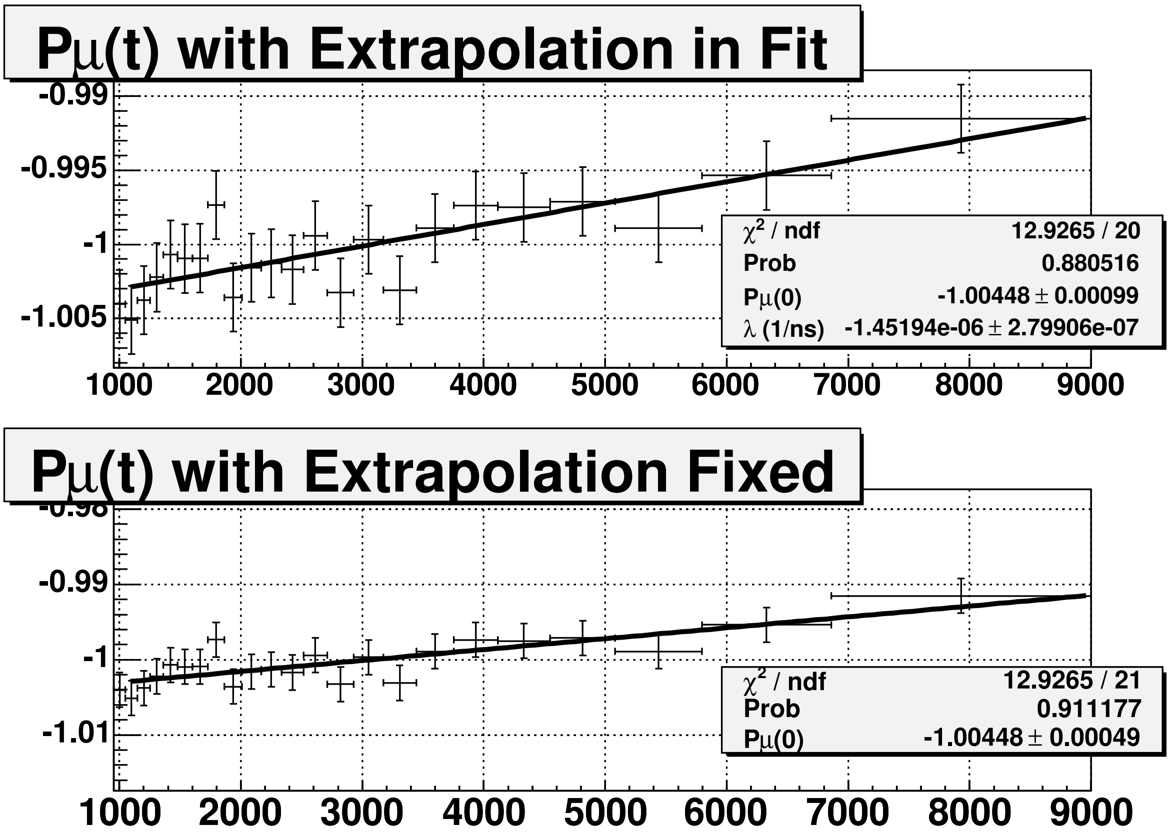

Figure 6.9: Plot of the polarization estimate from an asymmetry analysis of the 2004 data fit to an exponential with the slope as a fit parameter in the top figure, and with the slope fixed in the bottom figure.

6.1.5 Beam Intensity and Coincident Particles

To estimate a systematic uncertainty in $P_\mu\xi$ due to beam rate and coincident particles 2002 data was used. A spectrum fit of low rate data with a muon rate of 1.18kHz to high rate data with a muon rate of 4.7kHz yielded a $\Delta P_\mu\xi$ of $(-3.0 \pm 1.7)\times 10^{-3}$.

For 2004 data sets the rate was about 3kHz, and the worst case change in rate was 500 Hz. Since accidentals have a quadratic dependence, the scaling of the sensitivity is assumed to be quadratic also. The scale factor is: $[\frac{4.7}{1.2}\frac{3./2.5}{]}^{2} = 11$. The systematic uncertainty in $P_\mu\xi$ due to beam intensity is therefore -0.00027 ± 0.00003.

6.1.6 Proton Beam Stability

The movement of the muon beam when the proton beam on the production target was moved. The result is that $d\bar{y}_\mu/dy_p \approx 0.25$, and $d\bar{x}_\mu/dx_p \approx 0.5$. Movement of the proton beam by $\pm 1mm$ resulted in a change in the muon beam $\overline{dX}$ of $0.2mrad$, and the change in $\overline{dY}$ was less than $1.3mrad$

Monitoring of the beam position is done using roughly weekly low intensity target scans, where about $1\mu A$ of proton beam is steered both vertically and horizontally. Vertical steering of the protons is done with steering magnet labelled 1ASM4 (SM4), and horizontal steering with 1ASM5 (SM5). The calibration of the movement of the beam is with "protect monitor" plates located 2.5 mm to either side of the nominal proton beam steered centered. The setting of these steering magnets is monitored in our slow controls. The variation in position of the proton beam over the production data taking estimated from these history plots is 0.25mm vertically and 0.1mm horizontally.

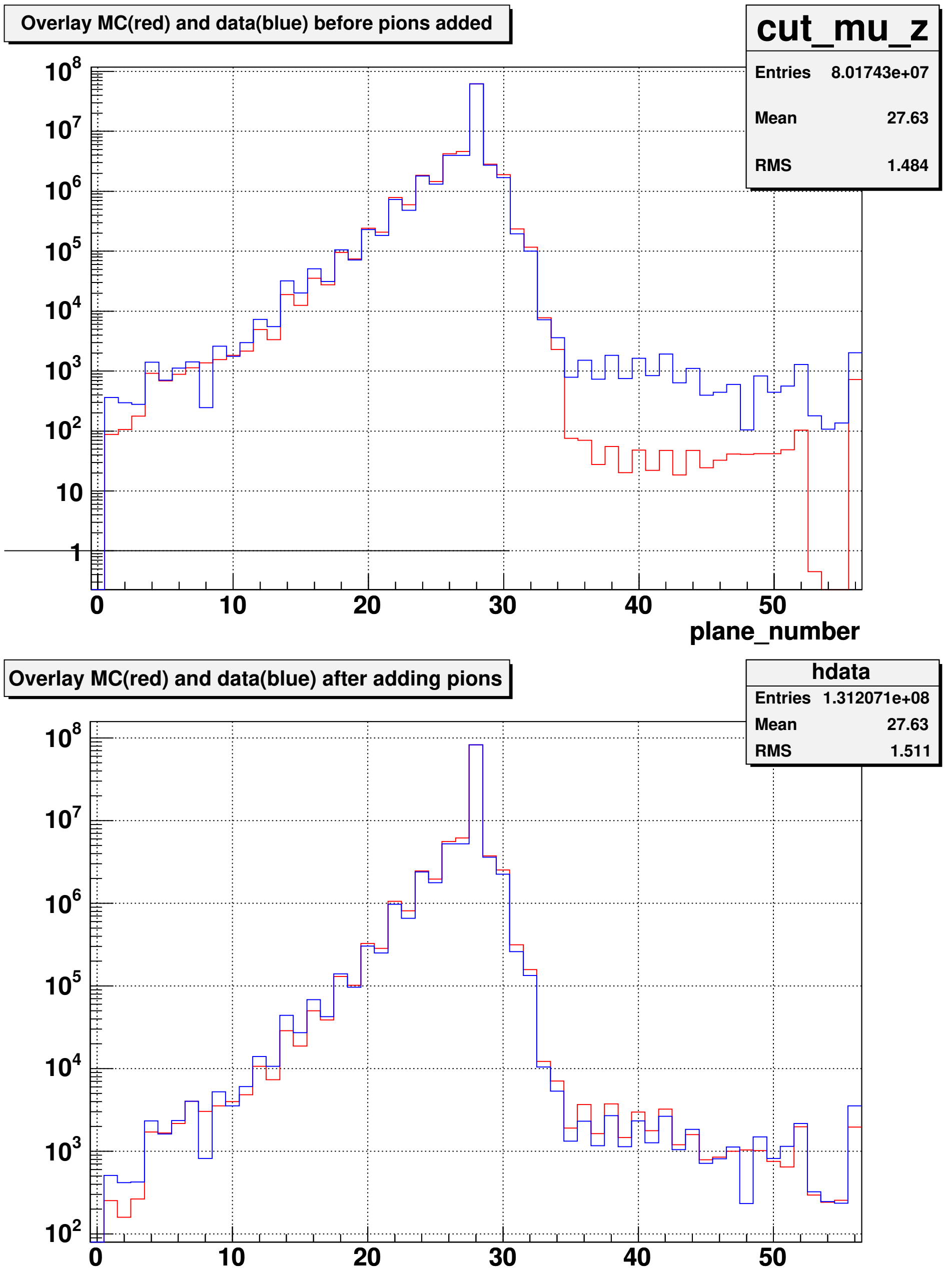

Figure 6.10: Overlay of the data set 35 and MC gen235 last plane hit histogram before adding muon stops from pions in the beam on the top. The same histograms but with pions added at the level of to the beam is shown on the bottom.

From these numbers, the maximum movement of the muon beam due to proton beam movements is 0.063mm vertically and 0.025mm horizontally. The change in angle of the muon beam due to proton beam movement is within 0.08$mrad$ vertically and 0.01$mrad$ horizontally. The systematic error due to these beam movements is estimated using a plot similar to Figure 6.5. The result is that the systematic error due to proton beam stability is $\pm 0.02 \times 10^{-3}$.

6.2 Systematic Uncertainty Due to Chamber Response

This section describes the systematic uncertainty due to the drift and proportional chamber response. The effects considered are: time variations in the wire to wire timing (t0 variations), changes in the space-to-time relations (STR) due to density variations, changes in the foil bulge due to changes in differential pressure between the chamber gas and He volume, the asymmetry of the wire positions relative to the foils due to construction, a deadzone due to a healing time after a muon passes through the chambers, and an upstream-downstream of the muon stopping target chamber efficiency difference.

Two other effects were considered, but were removed from the systematic uncertainty estimate because they were considered to be too small, or would introduce some double counting. The effects removed were DC and PC efficiency, and crosstalk removal.

6.2.1 Wire to Wire Time Variations

To estimate the possible time variation in the wire to wire time zero, calibration runs were taken at the beginning middle and end of the run period. The beginning and end calibration runs were taken with the magnetic field off with a single trigger, while the middle of run calibration was taken with the magnet on and with two different triggers. From these calibration runs three different calibration files were made. For the end of run calibration half of the chambers were missing, so for the missing planes times from a different beginning of the run time calibration run were used.

To measure the sensitivity of the muon decay parameters to t0 variations a calibration file shifted by ten times the difference in the beginning and end of run time calibrations was used. The large changes in time calibrations made the helix track fits have much worse χ^2. The value of Δ $P_\mu\xi$ obtained from fitting the exaggerated time shift analysis spectrum to a normal analysis spectrum was $(8.9 \pm 2.3)\times10^{-3}$. Resulting in a systematic error estimate of 0.89×10^{-3}.

Add possible third point to see if this scales quadratically?

6.2.2 Density Variations

Survey plots of density variation for each 2004 data set show that there are changes in density of as much as $\pm2\%$. To estimate the effect of density changes a set of MC was generated with the temperature changed by 10% (from 300K to 270K). A fit of the changed temperature MC to an ordinary MC gave a Δ $P_\mu\xi$ of $(2.4 \pm 1.4)\times10^{-3}$. This translates to a systematic uncertainty of 0.49×10^{-3}.

6.2.3 Chamber Foil Bulge

The shape of the chamber cathode foils depends on the differential pressure between the chamber gas and the He gas of the cradle holding all of the chambers. The differential pressure of the chambers was monitored and controlled by the gas system. To calibrate software measures of how much the foils bulged several nominal data runs were taken at different differential pressures. The average helix fit drift time difference for tracks that go through the center of the chambers relative to the average helix fit drift times for tracks that go through the radially distant part of the chamber was found to be sensitive to the foil bulge. Run to run monitoring of this fit time difference shows that the variation in foil bulge was controlled to better than $50\mu m$.

To measure the sensitivity of the muon decay parameters to the chamber foil bulge a set of MC was generated with the STR calibration changed as if the foils were moved outward by $500\mu m$. A fit of the decay positron spectrum from this exaggerated bulge to a nominal decay positron spectrum yielded Δ $P_\mu\xi$ of (2.2 ± 1.4) $\times10^{-3}$. The systematic uncertainty due to time variations in the foil bulge is estimated to be 0.22×10^{-3}.

6.2.4 Chamber Cell Asymmetry

Surveys of the constructed chambers show that the spacing between the wire plane and cathode foils was not the same on either side of the wire. On average the cathodes were found to be shifted by about $150\mu m$ from their nominal 2mm spacing from the wire planes. The position of the cathode foils was also determined using normal decay positron data with the magnet on. The technique used was to use the bulge calibration data from runs with different bulges to calibrate a time difference to a foil shift distance. The time difference looked at for the cathode foil position estimate was the difference between the average helix fit time in one half of the chamber cell to the average time in the other half of the chamber cell.

To investigate the effect of these cathode foil shifts, the as measured in software foil shifts were simulated in MC. STR files changed half-plane by half-plane to match the measured shifts. A fit of the muon decay distribution from the shifted cathode foil MC to a MC with symmetric planes gave a Δ $P_\mu\xi$ of $(-0.2 \pm 1.4)\times10^{-3}$. Since this shift of the cathode foils is thought to match the real detector, there is no scaling of this sensitivity, so the sensitivity is used as the systematic uncertainty.

6.2.5 Muon Deadzone

As the muon is brought through the upstream half of the detector to come to a stop in the stopping target, it deposits large ionization in the chambers. The resulting electron avalanch near the wires takes time to heal as the ions drift back to the cathode planes. The deadzone was measured by projecting helical fits to the decay positrons back to a wire that had a muon hit. For each muon hit the wire efficiency versus distance away from the muon hit is estimated as a function of time after the muon.

A measurement of the muon decay parameter sensitivities to the muon deadzone was made by introducing much larger and longer lived deadzone in a MC set than was observed in our data. A fit of this exaggerated deadzone decay positron MC to a spectrum from a MC run with no deadzone yielded a $P_\mu\xi$ sensitivity of $(0.2 \pm 1.4)\times10^{-3}$.

To get the scaling of the sensitivity a single run simulation with the deadzone as measured in data was done to count the number of hits removed by the deadzone. The number of hits removed from the exaggerated deadzone MC was also counted, and the estimate of the scaling was the ration of the hits in each of these runs. The resulting scaling factor was 11.7 for the PC where the muon stops, 25.8 for the DC chambers, and 47.6 for the far upstream PC's. A conservative estimate of the systematic uncertainty due to the muon deadzone is 0.01×10^{-3} using the scaling factor of 11.7.

6.2.6 Upstream versus Downstream Efficiency

The difference in the average number of degrees of freedom in the track fits in the upstream versus downstream for the same energy and angle is used to estimate an upstream/downstream efficiency difference. The difference between the upstream and downstream degrees of freedom in data versus in the data is 0.18 degrees of freedom. The average data and MC degrees of freedom for different decay positron momenta and angle are shown in Figures 6.11 and **??** respectively.

To estimate the sensitivity of the muon decay parameters due to a difference in upstream versus downstream efficiency a data set was analyzed with 5% of its downstream DC hits thrown away at the unpacking stage of analysis. This upstream downstream inefficiency change compared to a normal analysis of the same data gave a sensitivity of $(1.9 \pm 2.3)\times10^{-3}$ with a $\chi^2/NDOF = 283/1887$. Applying a correction to the error on the sensitivity reduces the error to $\pm0.9 \times 10^{-3}$.

The lowered efficiency run has about 1.8 dof less downstream than the standard run. Given that the difference between MC and data is 0.18 NDOF the scaling of the sensitivity is 10. The systematic uncertainty due to the difference in upstream and downstream efficiency is ergo 0.2×10^{-3}.

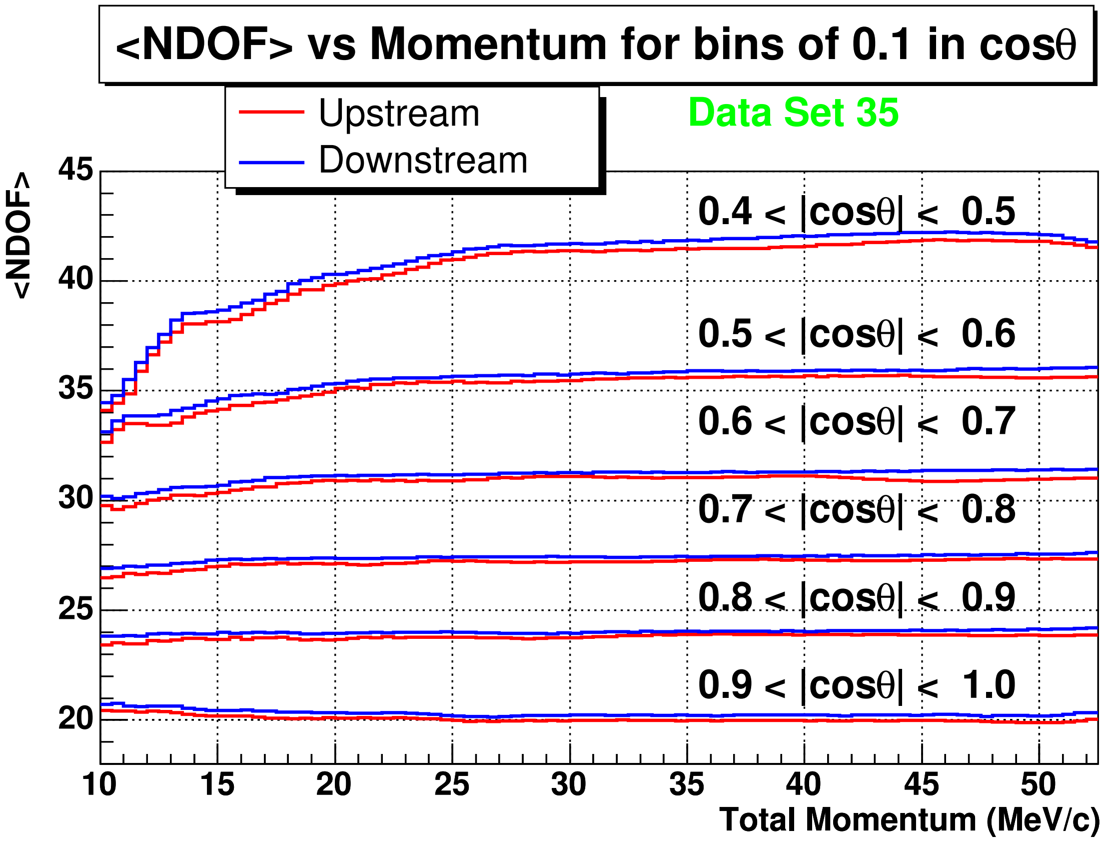

Figure 6.11: Mean helix fit number of degrees of freedom (NDOF) for Data versus momentum for different ranges of $\cos\theta$. The blue (or higher NDOF) of each $\cos\theta$ range is for upstream decay positrons, and the red (or lower NDOF) is for upstream decay positrons.

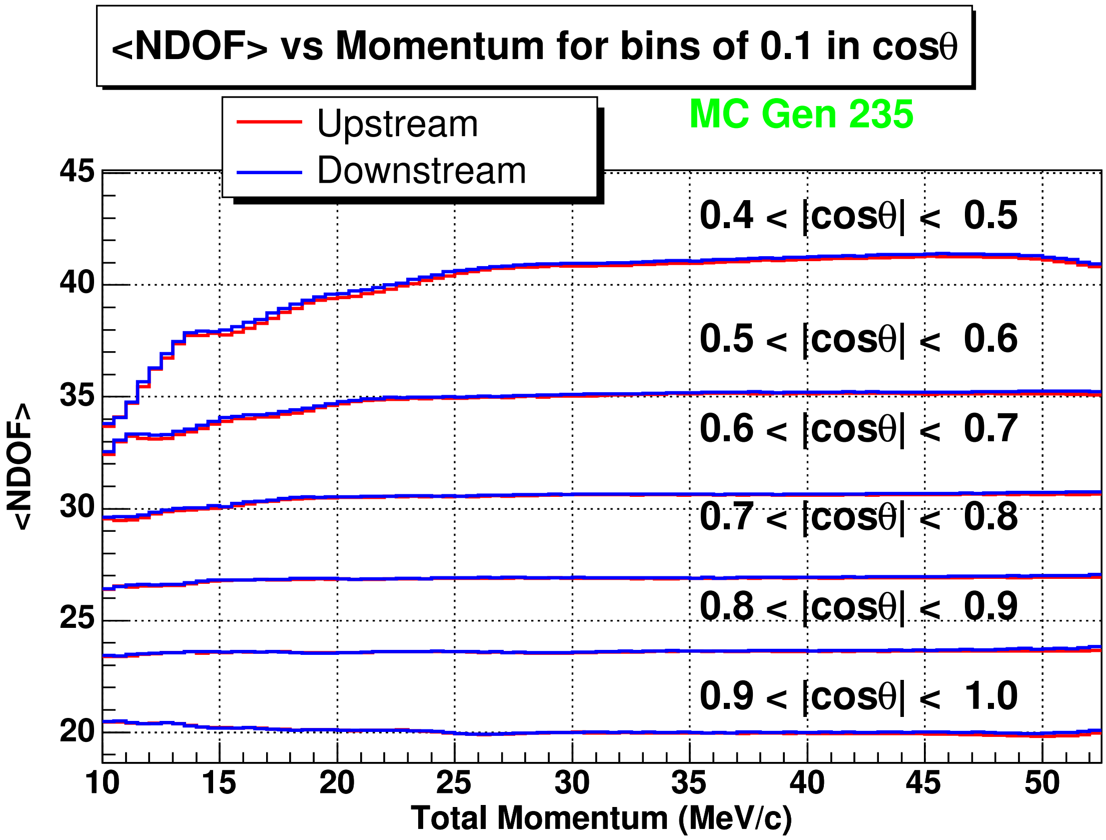

Figure 6.12: Mean helix fit number of degrees of freedom (NDOF) for MC versus momentum for different ranges of $\cos\theta$. The blue (or higher NDOF) of each $\cos\theta$ range is for upstream decay positrons, and the red (or lower NDOF) is for upstream decay positrons.

6.3 Systematic Uncertainty Due to Positron Interactions

The systematic uncertainty due to positron interactions includes three effects: a discrepancy between MC and data energy loss, hard and intermediate interactions, and back-scattering off of material ouside our detector.

6.3.1 Energy Loss

The largest positron interaction effect has to do with an unexplained difference of 10keV/c between our MC and data energy loss at the endpoint momentum. This 10 keV/c difference between upstream and downstream fits to straight through decay positrons is of the opposite sign to differences observed in our energy calibrations of MC and data so is not considered to be double counting.

The systematic estimate comes from looking at the energy calibration of a MC that had a thicker stopping target than nominal. The change in the energy calibration was also about 10keV/c resulting in a scaling factor of 1. The fit of the thick target to nominal target decay positron spectra resulted in the systematic error estimate 0.95×10^{-3}.

6.3.2 Hard Interactions

One of the positron interaction systematic errors has to do with how well we can validate the simulation of hard and intermediate interactions. Hard interaction events are arbitrarily defined here to be events in which the decay positron loses more than $1MeV/c$ of momentum from were it is generated to where it goes through the last DC. Intermediate interactions are those events whose decay positrons have lost less than $1MeV/c$.

In our simulation we can look at the reconstructed decay positron distribution over the thrown distribution to see how large a correction is needed to account for hard and intermediate interactions. The ratio of of reconstructed over thrown distributions in $\cos\theta$ for all events, events that lose $< 1MeV/c$, and those events that lose $> 1MeV/c$ is shown in Figure 6.13.

Muon decay spectrum fits of the reconstructed to thrown distributions for all events, and for events that lose less than $< 1MeV/c$ were done to estimate the size of correction. Plots of the change $P_\mu\xi$ is shown in Figure 6.14. Note that the sign needs to be flipped for the systematic because of the order the fit was done.

Fits of the hard interactions to the thrown distributions failed. To estimate the hard interaction contributions, the difference between fits to all events and fits to intermediate events is considered. The size of the corrections from the fit results are in Table 6.5 for $P_\mu\xi$. The size of the correction depends on the location of the muon stopping Bragg peak in the stopping target.

μ Location in Target	Δ $P_\mu\xi$ Inter.	Δ $P_\mu\xi$ Hard	Systematic Error
PC 5 stops (upstream)	-0.0125	0.0015	0.0006
centered ($\frac{1}{2}$)	-0.0068	-0.0037	0.0003
$\frac{3}{4}$	-0.0015	-0.0105	0.0001

Table 6.5: Δ $P_\mu\xi$ corrections due to intermediate and hard interactions for each of the three different muon stopping locations of data. The systematic error is based on 0.5% validation of hard interactions and 5% validation of intermediate interactions added in quadrature.

Given that our simulation is validated to 0.5% for hard interactions, and to 5% for intermediate interactions we obtain a systematic uncertainty in $P_\mu\xi$ of 0.3×10^{-3}. For plots and a description of the validation of our simulation refer to Chapter 4.

6.3.3 Material Outside the Detector

Materials outside of the tracking volume provided surfaces for the decay positrons to back-scatter from. In particular, components of the beam package were a source of decay particles, deltas and backscattered

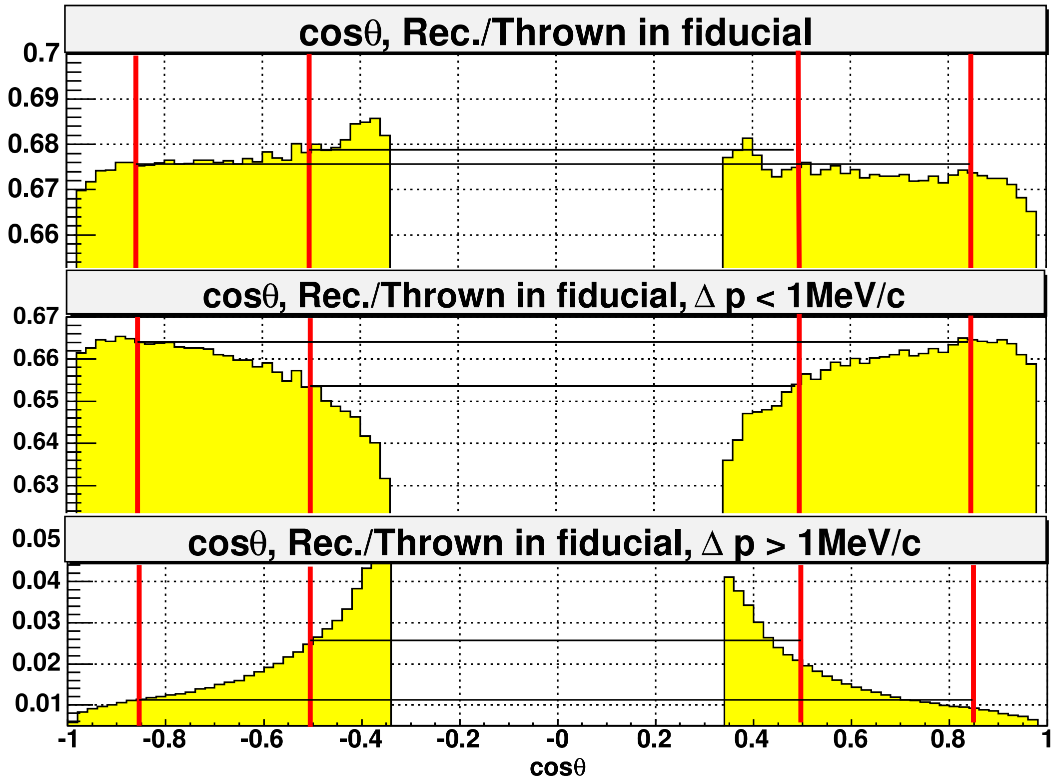

Figure 6.13: Reconstructed over thrown yield versus $\cos\theta$ for events in the fiducial $p_{total} < 50.0MeV/c$, $p_{trans} < 38.6MeV/c$, and $p_{long} > 13.7MeV/c$. The top plot is for all events, the middle plot is for events where the decay positron loses less than 1MeV/c, and the bottom plot is for positron energy loss greater than 1 MeV/c. The plots are for a muon stopping distribution centered in the target.

positrons. The systematic due to such extra particles was calculated by collecting a set of data with additional material introduced downstream of the detector.

The spectrum from data with extra material was fit to a spectrum from data without the extra material. The extra material added was an 0.65 cm thick aluminum plate was mounted on an 0.59 cm thick plastic plate about 80 cm downstream of the central stopping target. Monte Carlo simulations of the additional downstream material produced a spectrum that was fit to a spectrum from a nominal Monte Carlo set. The comparison of the two fits yields the difference in ξ due to inaccuracies in the Monte Carlo simulation of material outside the detector.

The effect is scaled by the ratio of extra particles due to the aluminum divided by the difference between data a nd Monte Carlo in nominal conditions.

$$\frac{R_i}{\sigma_i} = \frac{N_{Aluminum}^{Extra\ Particles}}{|N_{Data}^{Extra\ Particles} - N_{MonteCarlo}^{Extra\ Particles}|} = 60 \tag{6.8}$$

The sensitivity from the data to data spectrum fit is Δ $\mathrm{P}_\mu\xi = (1.2 \pm 1.4) \times 10^{-3}$. The resulting systematic uncertainty is 0.02×10^{-3}. Note that outside the nominal fiducial region differences between the MC and data backscattering has been observed. The difference is predicted to be due to backscattering off of the solenoid yoke which was not present in the production simulation. Plots showing the distribution of decay positron angle and energy for events identified as having a backscatter or beam positron correlated in time withthe decay positron are shown in Figure 6.15.

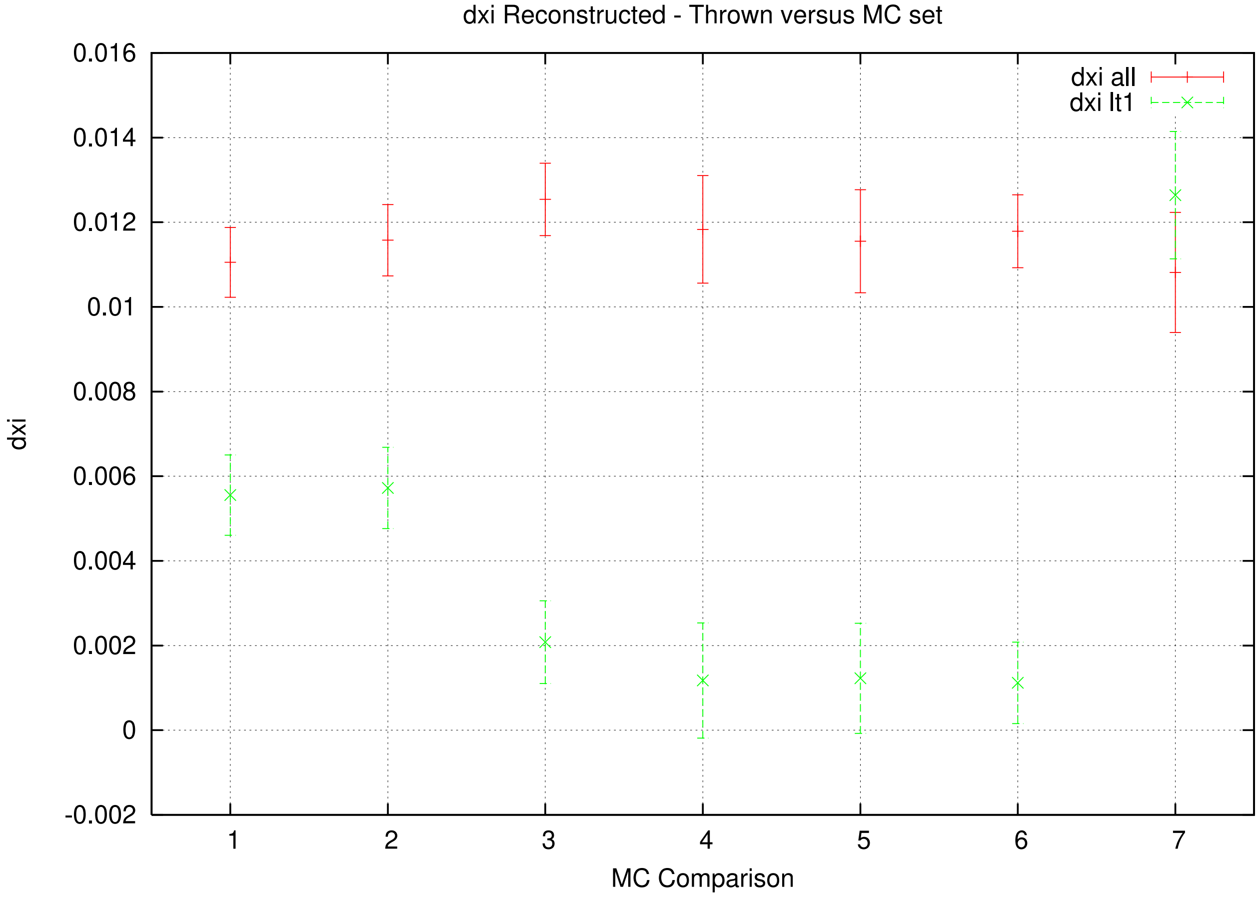

Figure 6.14: $\Delta\xi$ from spectrum fits to distributions of $\cos\theta$ versus total momentum of reconstructed to thrown decay positron distributions. Michel fits of all events to are shown as '+' and the fits to events with decay positrons that lose less than $1MeV/c$ are shown as 'x'. Points 1 and 2 are for muons stopping centered, points 3 to 6 are stopping at three-quarters, and point 7 is for muons stopping further upstream.

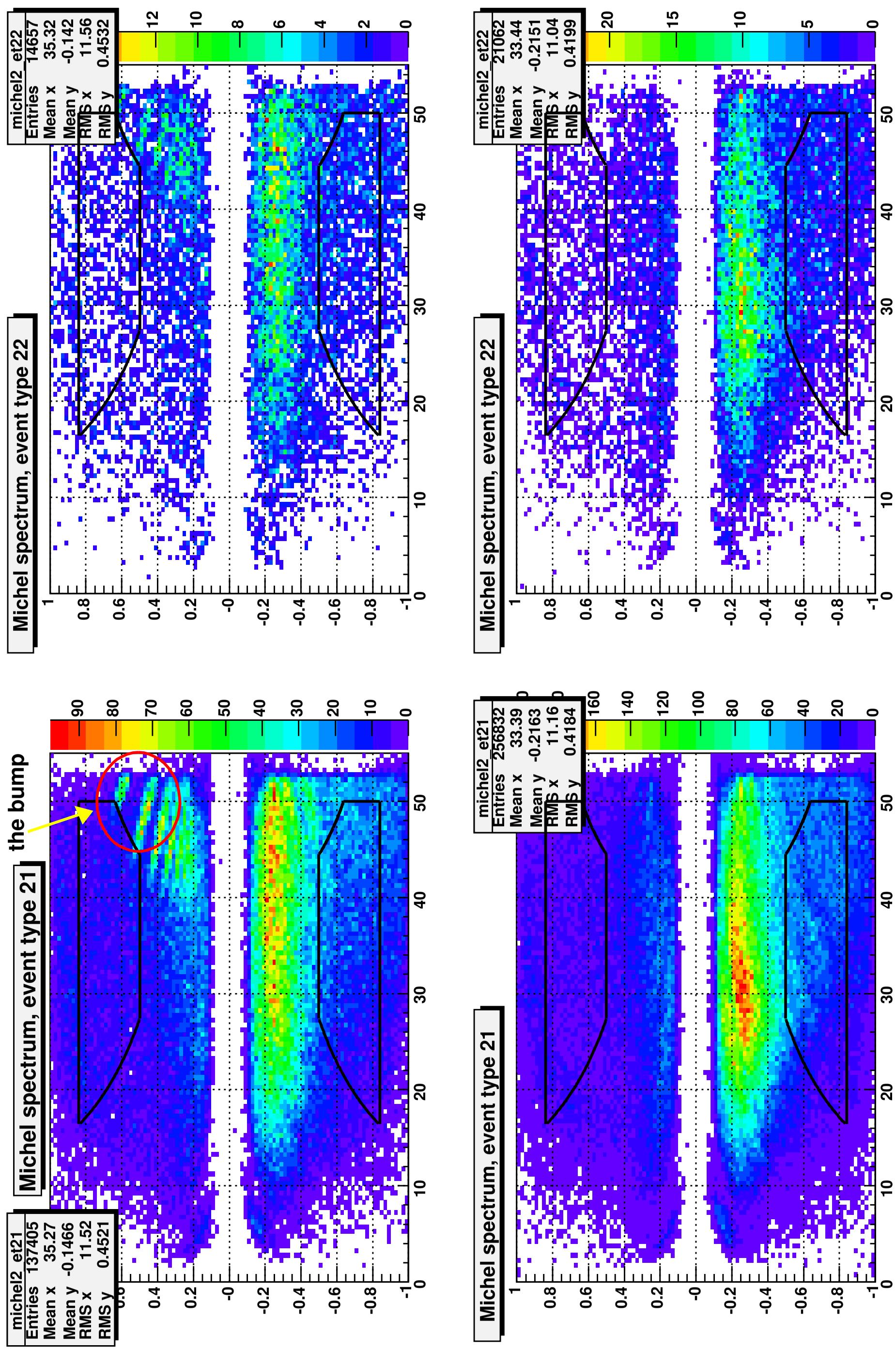

Figure 6.15: Plots showing the distribution of decay positron angle and energy for events identified as having a backscatter or beam positron correlated in time withthe decay positron. The top two plots are two different backscatter event types from data, and the bottom two plots are the same event types from the simulation.

6.4 Systematic Error Due to Spectrometer Alignment

The systematic uncertainty due to spectrometer alignment comes from how well the chamber translations in x, y, z and angle can be corrected to match their true positions. Also how well the misalignment between the magnetic field axis to the chamber axis is accounted for introduces some systematic uncertainty. The following subsections describe and quantify the systematic uncertainties related to the spectrometer alignment.

6.4.1 Longitudinal Alignment

The alignment of the planes in z is by construction. The spacing of the chambers was precisely measured and controlled by the special Sital spacers. The precision of the chamber spacing is $30\mu m$ longitudinally. To measure the sensitivity of the muon decay parameters to a longitudinal misalignment of the chambers random offsets of ten times the chamber spacing precision were introduced in the analysis of a MC set. The resulting systematic uncertainty in $P_\mu\xi$ is 0.22×10^{-3}.

6.4.2 Rotational Alignment

The rotational alignment systematic was found by analyzing a data set with an alignment file containing random rotational offsets 10 times the $0.01°$ precision of the rotational alignment corrections. The systematic uncertainty in the rotational alignment is 0.22×10^{-3}.

6.4.3 Magnetic Field Alignment

The accuracy of the alignment of the magnetic field axis to the chamber axis is $0.02mrad$, but the mismatch between upstream and downstream is $0.3mrad$ for 2003 data and $0.1mrad$ for 2004 data.

To measure the sensitivity a misalignment of the magnetic field of 0.25 degrees (4.4mrad) was introduced in the simulation. A fit of the reconstructed decay positron spectrum of the misaligned simulation to a nominal set gave a sensitivity of $(1.2 \pm 1.4) \times 10^{-3}$.

Using a scaling factor of 40 (4mrad/0.1mrad) for the 2004 data gives the systematic uncertainty of 0.03×10^{-3} due to misalignment of the magnetic field.

6.4.4 Translational Alignment

The translational alignment systematic effect was investigated by analyzing a nominal data set with an alignment file containing random translational offsets 28 times the 5 μm precision of the translational alignment corrections. The resulting spectrum fitting yields a systematic uncertainty on $P_\mu\xi$ of $< 0.01 \times 10^{-3}$.

6.5 Systematic Uncertainty Due to Momentum Calibration

The systematic uncertainty in momentum calibration comes from two contributions. One contribution is due to how well we can do our endpoint energy calibration. The other factor is how well our magnetic field map represents reality.

6.5.1 Endpoint fits

The method of doing endpoint fits to obtain a momentum calibration is presented in Section 3.5. The sensitivity to momentum calibration is measured by fitting a spectrum that has had the momentum calibration properly applied to a spectrum to a spectrum where one of the energy calibration parameters was shifted by 100keV/c.

The scaling factor for this sensitivity measure is taken to be the 100keV/c shift over the discrepancy between the MC and data endpoint calibrations since they should have come out to be the same. This results in a scaling factor of 10. The overall systematic uncertainty on $P_\mu\xi$ is 0.56×10^{-3}.

6.5.2 Magnetic Field Uniformity

Inaccuracies in the magnetic field map lead to inaccuracies in the determination of the decay positron momentum. To quantize this effect, a modified magnetic field map was produced by distorting the standard field simulation. The distortion took the form:

$$\Delta B_z = -(0.006\ G/cm^2)z^2 - (0.00004\ G/cm^3)z^3 - (1.25\ G/cm)r \tag{6.9}$$

A nominal data set was analyzed with the distorted field map, and the resulting decay positron spectrum was fit to the standard analysis of the same data set. The resulting sensitivity to $P_\mu\xi$ was $(-0.9 \pm 1.6) \times 10^{-3}$.

The distorted field map differs from the nominal 2T field map by up to 40G at the extremes of the tracking volume. Differences between an Opera generated field map, and the measured field map are 2G at the extremes of the tracking region. A conservative scaling factor of 10 gives a systematic uncertainty of 0.09×10^{-3}.